Supporting Information

Halide-Free Synthesis of Metastable Graphitic BC_3

Devin McGlamery[‡], Charles McDaniel[‡], Dylan M. Ladd[‡], Yang Ha[‖], Martín A. Mosquera[‡], Michael T. Mock[‡], and Nicholas P. Stadie[‡]*

‡ Department of Chemistry & Biochemistry, Montana State University, Bozeman, Montana 59717, United States

‖ Advanced Light Source, Lawrence Berkeley National Laboratory, Berkeley, California, 94720, United States

*Email: nstadie@montana.edu

Contents:

1. Synthetic Methods:

Direct Synthesis of BC_3 from BBr_3 (Route I). The idealized reaction in the previously established[1] direct synthesis of bulk BC_3 (referred to herein as route I) is:

$$2\ BBr_{3\ (l)} + C_6H_{6\ (l)} \rightarrow 2\ BC_{3\ (s)} + 6\ HBr_{(g)}$$

A 2:1 molar solution of boron tribromide (liquid, 99.99%, Sigma-Aldrich) and benzene (liquid, 99.8%, Sigma-Aldrich) was charged into a ~35 mL quartz ampule inside a glovebox under an inert argon atmosphere (<0.5 ppm of H_2O, <0.5 ppm of O_2). The total volume of solution added was 313 µL, limiting the maximum pressure to <20 bar at 800 °C. The open end of the ampule was closed with a Swagelok Ultra-Torr adapter and removed from the glovebox. The lower half of the ampule was submerged in liquid nitrogen to solidify the precursors. In this state, the ampule was connected to a stainless-steel Schlenk line, evacuated to 10^{-2} mbar, and flame-sealed under active vacuum. The sealed ampule was then placed in the center of a chamber furnace (RWF 12/13, Carbolite Gero Ltd.) and heated to 800 °C at 1 °C min^{-1}. The ampule was held at 800 °C for 1 h and then allowed to gradually cool to ambient temperature. The ampule was carefully scored with a diamond-bladed saw and snapped open within a nitrile rubber enclosure, releasing the over-pressure of gaseous byproducts into a fume hood. The solid product was collected and washed three times with deionized water, washed three times with acetone, and finally dried in air at 80 °C. The as-synthesized flakes (referred to herein as BC_3, reflecting their nominal composition) were in some cases investigated without further manipulation; in other experiments, they were reduced to powder by grinding in a dry mortar and pestle for 15 min, as denoted below.

Synthesis of BC_3 from B_2H_6 (Route II). A novel synthesis route to BC_3 via B_2H_6 as the boron precursor (route II) was carried out, based on the following idealized reaction:

$$B_2H_{6\,(g)} + C_6H_{6\,(l)} \rightarrow 2\,BC_{3\,(s)} + 6\,H_{2\,(g)}$$

A stainless-steel reactor (4651 high-pressure vessel, Parr Instrument Company) with a gas inlet port and an internal volume of 250 mL was thoroughly dried in air at 80 °C. A stainless-steel gasket (44HC7AD, Parr Instrument Company) was placed in the pre-lubricated sealing groove of the reactor body and all components were then transferred into a glovebox under inert argon atmosphere (<0.5 ppm of H_2O, <0.5 ppm of O_2); the reactor was charged with 0.62 mL of benzene (liquid, 99.8%, Sigma-Aldrich), sealed using a torque wrench, and transferred out of the glovebox. The main body of the sealed reactor was cooled by submersion in an acetone and dry ice bath for 60 min. It was then connected to a previously dried and evacuated gas/vacuum manifold via a metal gasket face-seal fitting (VCR, stainless steel, Swagelok Co.) and evacuated for 10 s using a dry scroll vacuum pump (10^{-2} mbar ultimate pressure, ACP 15, Pfeiffer Vacuum GmbH). After a brief evacuation, a gas mixture containing 30% diborane in hydrogen (99.99% purity B_2H_6 in 99.9999% purity H_2, Air Liquide Electronics U.S. LP) was filled into the reactor headspace up to a pressure of 2.0 bar (6.6 mmol or 180 mg of diborane). The reactor was then resealed, disconnected from the gas/vacuum manifold, removed from the cooling bath, and allowed to warm to room temperature. After thorough drying of the outer walls from condensation, the reactor was placed within a custom chamber furnace (Parr Instrument Company) and heated to 700 °C at 1 °C min^{-1}. The reactor was held at 700 °C for 4 h and then allowed to gradually cool to ambient temperature. During pyrolysis, the pressure within the closed reactor was monitored using an integrated transducer (G2, Ashcroft Inc.). Upon completion, the gaseous byproducts were vented into a fume hood to just above ambient pressure. The reactor was transferred into an argon glovebox and opened, and the product was collected from the bottom of the vessel; the solid product was investigated without further manipulation.

Safety Note (Route II). Diborane is a pyrophoric compound and is also toxic at low concentrations (LC50 values for inhalation at <100 ppm). Therefore, it is crucial that any gas manifold exposed to diborane at greater than atmospheric pressure (e.g., 2 bar) be leak-tight and sufficiently purged with argon prior to the introduction of diborane to remove any trace water or oxygen. Leak testing at elevated pressures using pure hydrogen or helium and a suitable leak detector (used herein with H_2: Sensistor XRS9012, INFICON Inc.) is highly recommended prior to introducing diborane to the system. Abatement is also crucially important; in this work, all waste diborane contained within the manifold (i.e., which was not closed within the reactor) was quenched by exhausting through a series of two Dreschel washing flasks filled with methanol at a flow rate of 20 sccm (see **Figure S4**). The system was then completely purged of diborane by flushing with excess argon at 100 sccm for 30 min.

Experimental Setup (Route II). A stainless-steel reactor equipped with a pressure transducer was custom-designed and fabricated over three versions to carry out synthesis route II. The ultimate design comprised a 250 mL reactor outfitted with a digital pressure transducer, allowing for monitoring and post-synthesis analysis of the reaction. By converting the pressure to a total amount of gaseous species present (using the ideal gas law and the known fixed volume and temperature), leaks and/or the change in amount of gaseous species could be plotted as a function of time (**Figure S1**). In the co-pyrolysis of diborane with benzene, analysis of the pressure profile reveals three distinct steps: (1) gasification of benzene, (2) decomposition of diborane followed by condensation of higher-order boranes, and (3) decomposition of benzene. In the neat pyrolysis of benzene, only two steps are observed: (1) gasification of benzene and (3) decomposition of benzene.

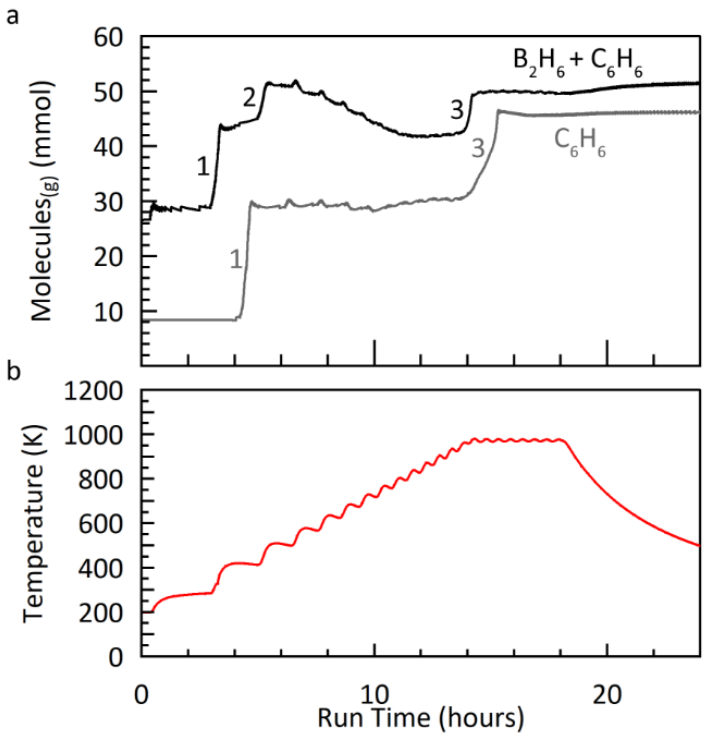

Figure S1. Gas evolution during pyrolysis in a custom metal reactor. (a) Change in amount of gaseous species present as a function of reaction time during the co-pyrolysis of B_2H_6 and C_6H_6 (route II) or pure C_6H_6, under closed, inert conditions and (b) the corresponding temperature profile.

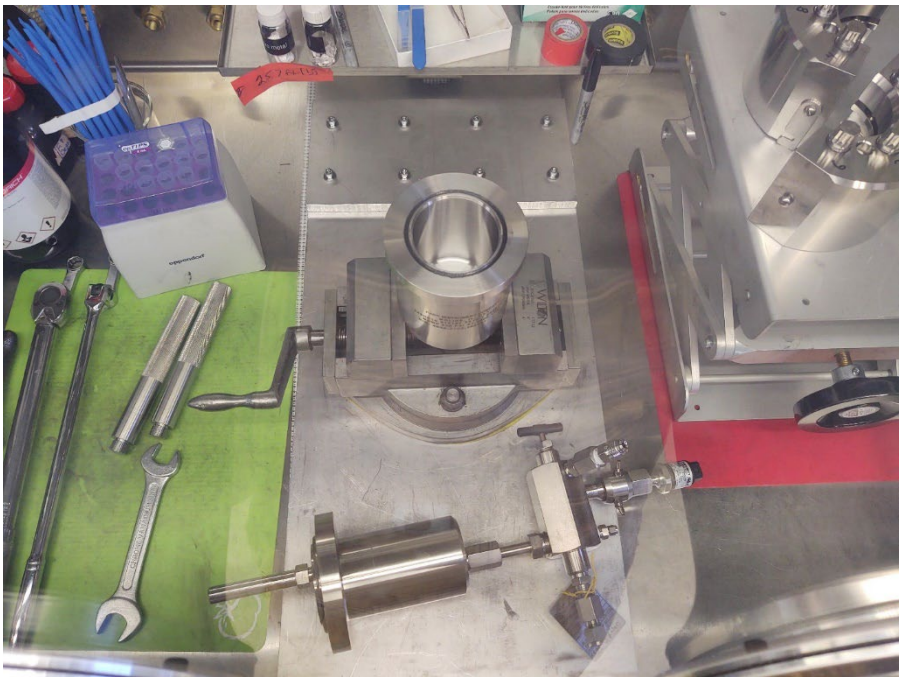

Figure S2. Experimental apparatus for filling and sealing the custom metal reactor within a glovebox: the reactor body affixed to a vise (center), the head of the reactor (bottom center), and the split-ring sealing cuff (top right) are shown.

Figure S3. Experimental apparatus for storage and delivery of diborane: lecture bottle containing the B_2H_6/H_2 mixture (center) within a freezer held at -20 °C, a purgeable regulator (right), pressure transducer controller (top center), and purge, vent, and delivery gas lines (right and top right) inside a fume hood.

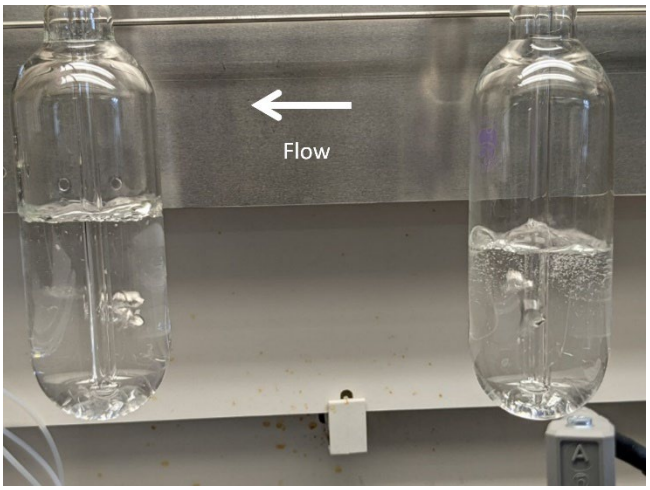

Figure S4. Experimental apparatus for diborane abatement: two Dreschel flasks (left and right) filled with methanol (clear liquid) showing exhaust flow from right to left. In contact with methanol, diborane is converted into trimethoxyborane and hydrogen is evolved (small bubbles are shown in both flasks, but less evolution occurs in the downstream flask on the left).

Figure S5. Experimental apparatus for diborane/benzene co-pyrolysis reactions (route II): custom metal reactor (center), furnace (center right), freezer containing the B_2H_6/H_2 mixture (left), purgeable regulator (center left), gas manifold (Teflon and stainless steel), vacuum outlet (right), and abatement system (top center). The reactor is shown submerged in an acetone and dry ice bath at -78 °C.

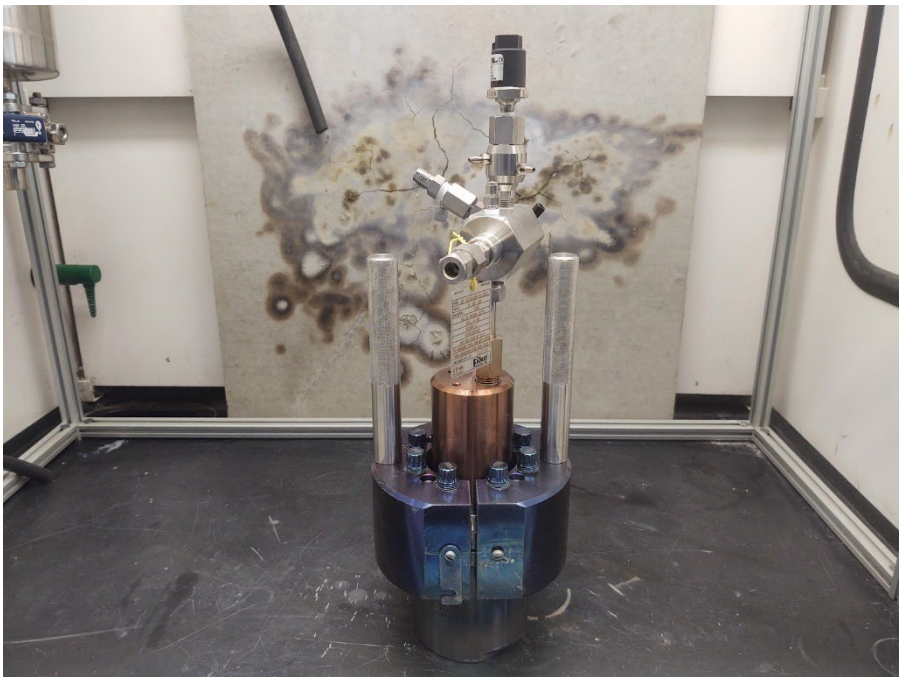

Figure S6. Custom metal reactor removed from the furnace, shown post reaction and prior to opening.

Figure S7. Custom metal reactor head and thermowell, shown post reaction (benzene pyrolysis at 700 °C) and after opening.

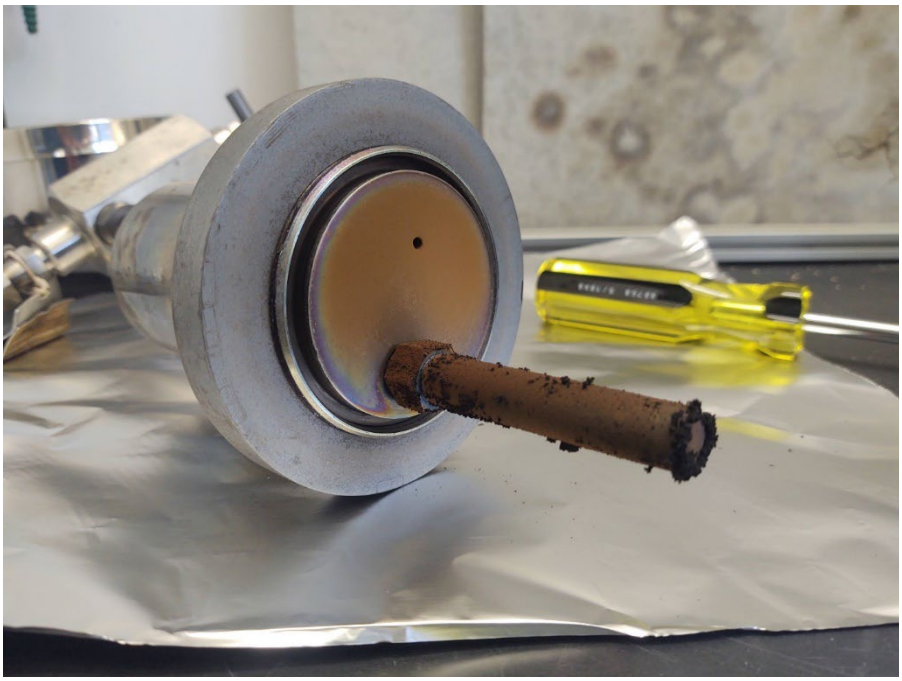

Figure S8. Custom metal reactor head and thermowell, shown post reaction (diborane/benzene pyrolysis at 700 °C) and after opening.

Synthesis of BC_3 from $B_{10}H_{14}$ (Route III). A novel synthesis route to BC_3 via $B_{10}H_{14}$ as the boron precursor (route III) was carried out, based on the following idealized reaction:

$$B_{10}H_{14\,(s)} + 5\,C_6H_{6\,(l)} \rightarrow 10\,BC_{3\,(s)} + 22\,H_{2\,(g)}$$

A 1:5 molar solution of decaborane (solid, technical grade, Sigma-Aldrich) and benzene (liquid, 99.8%, Sigma-Aldrich) was charged into a ~12 mL quartz ampule inside a glovebox under an inert argon atmosphere (<0.5 ppm of H_2O, <0.5 ppm of O_2). The total volume of solution added was 40 µL, limiting the maximum pressure to <20 bar at 800 °C. The open end of the ampule was closed with a Swagelok Ultra-Torr adapter and removed from the glovebox. Pyrolysis was carried out in an identical procedure as described in route I. The solid product was collected and washed three times with deionized water, washed three times with acetone, and finally dried in air at 80 °C. The as-synthesized flakes (referred to herein as BC_3, reflecting their nominal composition) were in some cases investigated without further

manipulation; in other experiments, they were reduced to powder by grinding in a dry mortar and pestle for 15 min, as denoted below.

Synthesis of NDB (Route IV Precursor). Methods to synthesize 1,8-naphthalenediyl-bridged diborane(6) (NDB) were adapted from those reported by Scholz and coworkers.[2] The materials, general procedures, and multi-step synthesis of NDB that were used herein follow.

Organic Synthesis Materials. Me_3SiCl and $B(OMe)_3$ were distilled over CaH_2 and Na, respectively. The following reagents were purchased from commercial vendors and used as received: $CDCl_3$ (99.8%, Cambridge Isotope Labs), 1,8-diiodonaphthalene (≥98.0%, Sigma Aldrich), *n*-BuLi (1.5 M in *n*-hexane, Thermo Scientific), CH_2Cl_2 (>99.9%, Honeywell), KOH (97.8%, Mallinckrodt Chemicals), HCl (Acros Organics), $MgSO_4$ (Oakwood Products, Inc.), $LiAlH_4$ (1.0 M in Et_2O, Sigma Aldrich). C_6D_6 was purchased from Cambridge Isotope Labs, degassed by three freeze-pump-thaw cycles, and stored in a N_2- or Ar-filled glovebox over activated molecular sieves.

Organic Synthesis General Procedures. All synthetic procedures were performed under N_2 or Ar using standard glovebox or Schlenk line techniques, unless otherwise noted. The solvents used for synthetic procedures (diethyl ether, Et_2O, and *n*-hexane) were sparged and stored under ultrahigh purity (UHP) Ar before being dried via passing through a solvent purification system (CHEMBLY, formerly JC Meyer Solvent Systems) using UHP argon as the working gas. All glassware was heated to 160 °C overnight prior to use.

NMR Spectroscopy. NMR spectra were measured at 298 K using a Bruker ASCEND AVANCE III HD 500 MHz (500.2 MHz for ^1H) spectrometer equipped with a Prodigy (liquid nitrogen cooled) cryoprobe or a Bruker UltraShield DPX AVANCE I 300 MHz spectrometer equipped with a room temperature QNP probe. ^1H NMR chemical shifts (δ in ppm) are referenced to residual ^1H solvent resonances in the deuterated solvent ($^1H/^{13}C$, C_6D_6: δ = 7.16/128.06). NMR signals abbreviations: s = singlet, d = doublet, dd = doublet of doublets, q = quartet, sept = septet, br = broad.

Synthesis of 1,8-Naphthalic Boronic Acid Anhydride, 1.

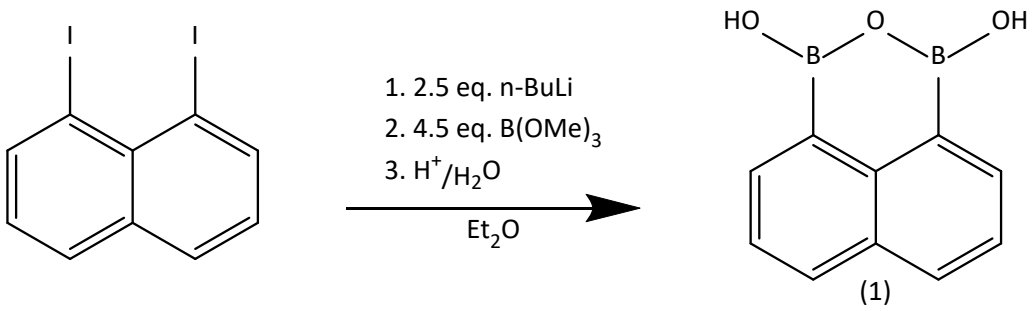

(1)

1,8-Diiodonapthalene (5.0 g, 13.13 mmol, 1 eq.) was added to a 250 mL Schlenk flask containing a stir bar. The solid was dissolved in dry Et_2O (~80 mL) and the solution was cooled to 0 °C. In this state, *n*-BuLi (1.5 M in *n*-hexane; 21 mL, 31.5 mmol, 2.5 eq.) was added dropwise via a syringe while the solution was stirred. The solution was allowed to warm to room temperature over the course of 3 h after which it was cooled to -78 °C and $B(OMe)_3$ (7.1 mL, 63 mmol, 4.5 eq.) was added dropwise. The solution was removed from the cooling bath and allowed to warm to room temperature over the course of 12 h. HCl (2 M in H_2O; 23.5 mL) was added, and the solution was stirred for an additional 2 h at room temperature. The two phases were separated, and the aqueous phase was extracted with CH_2Cl_2 (4×10 mL). The organic phases were combined and **1** was extracted into aqueous KOH (2 M; 4×10 mL). The aqueous phases were combined and washed with CH_2Cl_2. HCl (33 M in H_2O) was added dropwise to the aqueous phase until the solution became acidic, whereupon a precipitate formed. The precipitate was collected by vacuum filtration and washed with H_2O on the frit. The solid product was dissolved in ethyl acetate and dried over $MgSO_4$. The solution was filtered and the filtrate was obtained as an off-white solid by drying under reduced pressure to yield **1** (1.95 g, 9.87 mmol, 74% yield). **^{1}H NMR (300 MHz, $CDCl_3$):** δ = 8.20 (dd, 3J(H,H) = 6.8 Hz, 4J(H,H) = 0.9 Hz, 2H), δ = 8.06 (dd, 3J(H,H) = 8.3 Hz, 4J(H,H) = 0.9 Hz, 2H), δ = 7.60 (dd, 3J(H,H) = 8.3 Hz, 3J(H,H) = 6.8 Hz, 2H), δ = 4.75 (br, 2H; O–H).

Synthesis of 1,8-Naphthalenediyl-Bridged Diborane(6) (NDB).

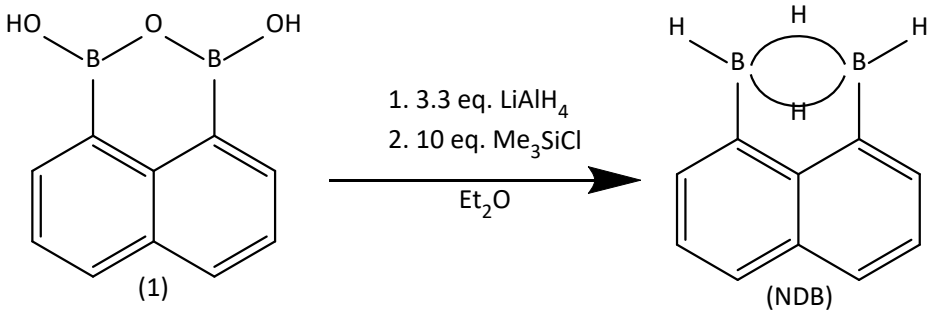

1 (0.5 g, 2.53 mmol, 1 eq.) was added to a 100 mL Schlenk flask equipped with a stir bar. The solid was dissolved in dry Et_2O (~50 mL) and cooled to 0 °C. In this state, a solution of $LiAlH_4$ (1M in Et_2O, 8.4 mL, 8.4 mmol, 3.3 eq.) was added dropwise via a syringe while the solution was stirred, during which a colorless precipitate formed along with the evolution of a colorless gas. The solution was stirred for 30 min at 0 °C then allowed to warm to room temperature where it was stirred for an additional 12 h. The solution was cooled to -78 °C and neat Me_3SiCl (3.2 mL, 25.3 mmol, 10 eq.) was added dropwise via a syringe, resulting in the formation of a colorless precipitate. The mixture was stirred for 10 min at -78 °C then allowed to warm to room temperature where it was stirred for an additional 12 h. The mixture was evaporated under reduced pressure to a yellow paste. This paste was thoroughly triturated with *n*-hexanes to assist in the removal of coordinated solvent molecules, then evaporated to dryness under reduced pressures. The NDB product was isolated in high purity by three subsequent vacuum sublimations (80 °C, 10^{-2} mbar) and collected as a clear crystalline sublimate to yield NDB (245 mg, 1.61 mmol, 64% yield). **^{1}H NMR (500 MHz, C_6D_6):** δ = 7.87 (d, 3J(H,H) = 6.7 Hz, 2H), δ = 7.71 (dd, 3J(H,H) = 8.3 Hz, 4J(H,H) = 0.6 Hz, 2H), δ = 7.38 (dd, 3J(H,H) = 8.3 Hz, 3J(H,H) = 6.7 Hz, 2H), δ = 4.78 (q, 1J(H,B) ≈ 130 Hz, 2H), δ = 1.61 (s, br, 2H). **^{13}C NMR (125 MHz, C_6D_6):** δ = 144.8, δ = 138.7 (br), δ = 133.5, δ = 130.0, δ = 130.0, δ = 126.9.

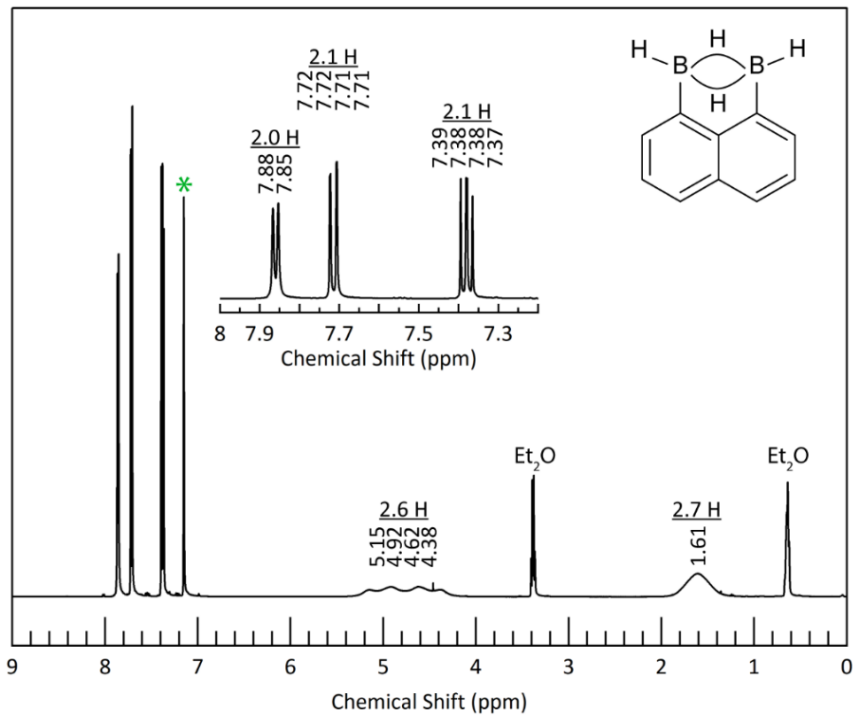

Figure S9. ^{1}H NMR spectrum of NDB dissolved in C_6D_6 (*) using a 500 MHz spectrometer.

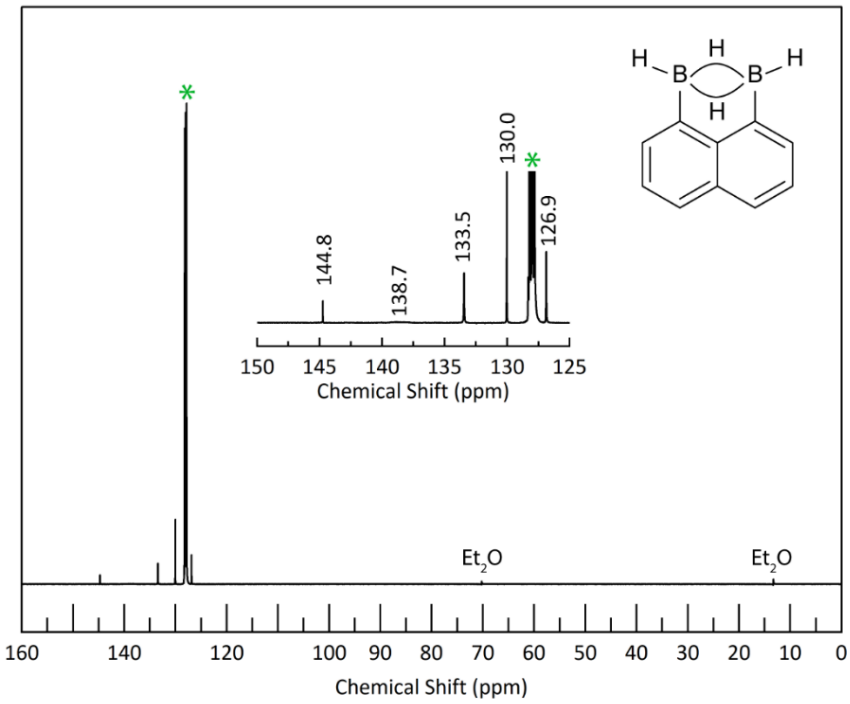

Figure S10. ^{13}C NMR spectrum of NDB dissolved in C_6D_6 (*) using a 500 MHz spectrometer.

Synthesis of BC_5 from the Molecular Tile $B_2C_{10}H_{10}$ (Route IV). A novel synthesis route to BC_5 via the neat pyrolysis of 1,8-naphthalenediyl-bridged diborane(6) (NDB, $B_2C_{10}H_{10}$, route IV) was carried out, based on the following idealized decomposition reaction:

$$B_2C_{10}H_{10\,(s)} \rightarrow 2\,BC_{5\,(s)} + 5\,H_{2\,(g)}$$

The product was purified three times by sublimation and then charged into a ~30 mL quartz ampule inside a glovebox under an inert argon atmosphere (<0.5 ppm of H_2O, <0.5 ppm of O_2). The total amount of NDB added was 200 mg, limiting the maximum pressure to <20 bar at 800 °C. The open end of the ampule was closed with a Swagelok Ultra-Torr adapter and removed from the glovebox. Pyrolysis was carried out in an identical procedure as described in routes I and III. The solid product was collected and washed three times with deionized water, washed three times with acetone, and finally dried in air at 80 °C. The as-synthesized material (referred to herein as BC_5, reflecting its nominal composition) was in some cases investigated without further manipulation; in other experiments, it was reduced to powder by grinding in a dry mortar and pestle for 15 min, as denoted below.

Separation of Pyrolysis Products. Upon pyrolysis of the NDB precursor, two morphologies were generated and separated by density. The minor flakes were suspended in ethanol and poured off while the majority solid (see **Figure S11**) was collected for further characterization.

Figure S11. Two solid products generated by the pyrolysis of $B_2C_{10}H_{14}$ (NDB) at 800 °C (route IV) can be seen: a suspension of flakes (left) and the remaining mound of the majority solid (right).

Synthesis of BC_3 from $NaBH_4$ (Route V). A novel synthesis route to BC_3 via $NaBH_4$ as the boron precursor (route V) was carried out, based on the following idealized reaction:

$$2\ NaBH_{4\ (s)} + 2\ I_{2\ (s)} + C_6H_{6\ (l)} \rightarrow 2\ BC_{3\ (s)} + 2\ NaI_{(s)} + 6\ H_{2\ (g)} + 2\ HI_{(g)}$$

Sodium borohydride (powder, 99%, Sigma-Aldrich), iodine (solid crystals, >99%, purified by sublimation, Sigma-Aldrich), and benzene (liquid, 99.8%, Sigma-Aldrich) were charged into a ~35 mL quartz ampule inside a glovebox under an inert argon atmosphere (<0.5 ppm of H_2O, <0.5 ppm of O_2). A typical mixture contained 65.5 mg of $NaBH_4$, 439.9 mg of I_2, and 77.2 µL of C_6H_6 to achieve a nominal stoichiometry of BC_3 at <20 bar at 800 °C. The open end of the ampule was closed with a Swagelok Ultra-Torr adapter and removed from the glovebox. Pyrolysis was carried out in an identical procedure as described in routes I, III, and IV. The solid product was collected and washed three times with deionized water, three times with acetone, once with a 50% aqueous HF solution, three additional times with deionized water, and finally three additional times with acetone; this product was dried in air at 80 °C.

The addition of elemental iodine to synthesis route V was necessary for the scavenging of sodium. While other sodium scavengers could be used (e.g., Se or Te), iodine was chosen herein. The decomposition of sodium borohydride in the presence of iodine produces reactive borane species at high temperatures that can be incorporated into the forming graphitic material to form BC_3. This is accompanied by the formation of sodium iodide (NaI) as a byproduct that can easily be separated from the reaction products by washing with water. The presence of any remaining sodium iodide in the product of route V is detectible by XRD. Upon further washing, the sodium iodide can be completely removed. The mother liquor from an aqueous wash was dried by evaporation to produce a white solid; analysis of this water-soluble solid is shown in **Figure S12**.

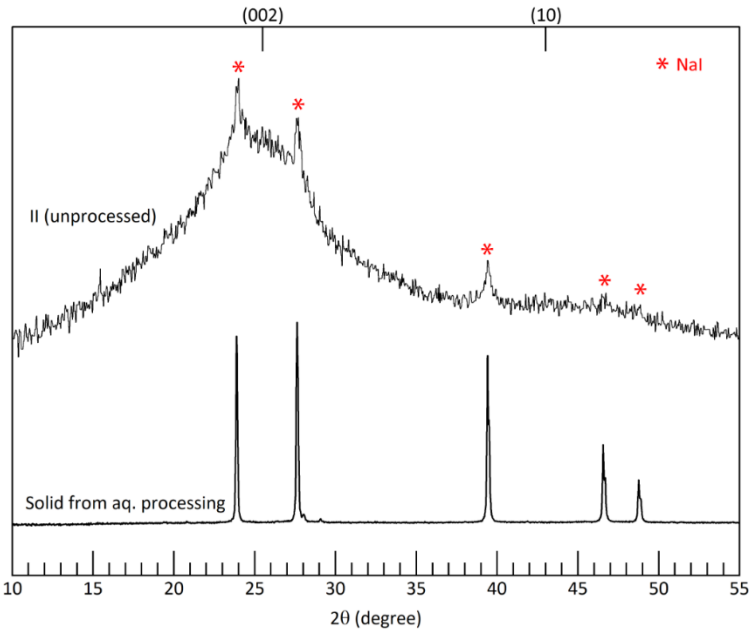

Figure S12. XRD patterns of the as-collected solid products generated by the co-pyrolysis of $NaBH_4$, I_2, and C_6H_6 under inert conditions within a quartz ampule at 800 °C (route V), and of the solid recovered after concentrating wash water from processing the graphitic material.

Compositional mapping of the as-synthesized product of synthesis route V via EDX reveals a mixture of boron-doped graphite, sodium iodide crystals, and sodium silicate fibers (see **Figure S13**). The sodium silicates can be effectively separated from the graphitic product by dissolution in hydrofluoric acid.

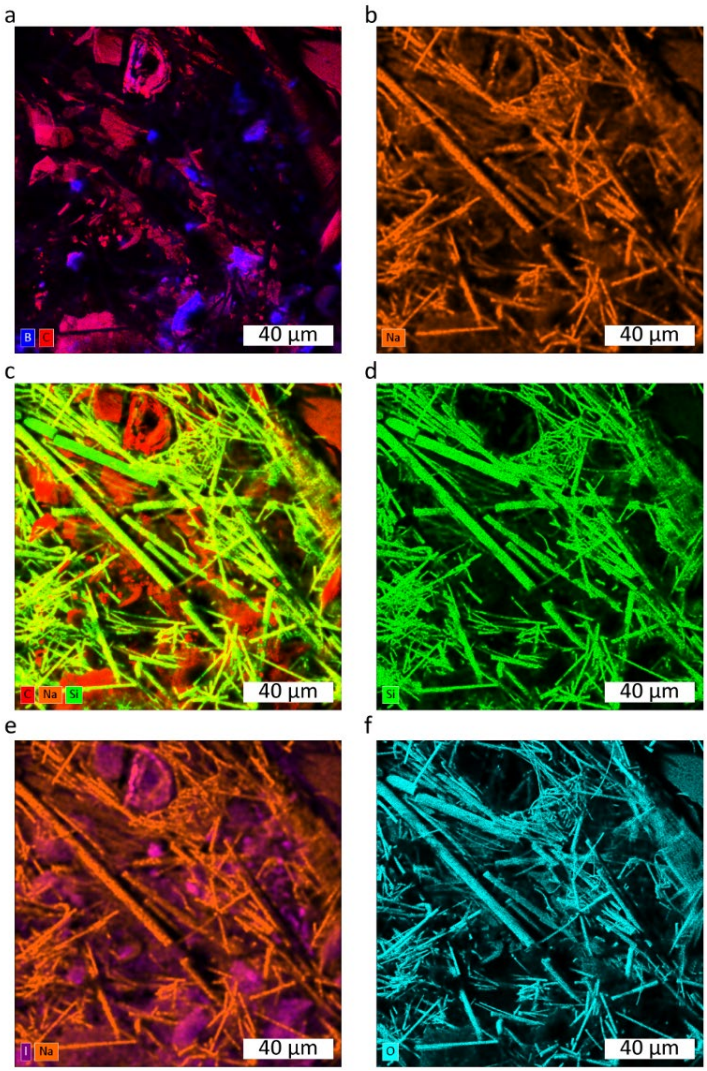

Figure S13. EDX maps of the as-collected solid products generated by the co-pyrolysis of $NaBH_4$, I_2, and C_6H_6 at 800 °C (route V). The color-coded maps are generated from the signals of (a) boron and carbon, (b) sodium, (c) carbon, sodium, and silicon, (d) silicon, (e) iodine and sodium, and (f) oxygen.

2. Characterization Methods:

X-Ray Diffraction. Powder X-ray diffraction (XRD) was performed on hand-ground samples using a laboratory diffractometer (D8 ADVANCE, Bruker Corp.) equipped with a Cu $K\alpha_{1,2}$ radiation source (λ = 1.54 Å) in reflection geometry. All measurements were performed at room temperature using a recessed-well sample holder (25 mm diameter well, Bruker Corp.); the sample was rotated at 15 rev min^{-1} and sampled in 0.02° increments for 0.5 s each from 2θ = 10°–60°.

Raman Spectroscopy. As-synthesized materials were investigated with a benchtop Raman spectrometer (LabRAM HR Evolution, Horiba Scientific Ltd.) equipped with a confocal microscope and three excitation sources: a 532 nm (2.33 eV) frequency doubled Nd:YAG laser with an incident power of 10 mW, a 633 nm (1.96 eV) HeNe laser with an incident power of 17 mW, and a 785 nm (1.58 eV) diode laser with an incident power of 25 mW. All measurements were performed at room temperature.

Fitting Raman Spectral Data. The region containing peaks associated to the D and G modes in each Raman spectrum were fitted using a previously established method based on the combination of a Lorentzian and a Breit-Wigner-Fano (BWF) lineshape.[3,4] The main D peak was fitted to a single Lorentzian and the low frequency shoulder of the D peak was fitted to another Lorentzian to account for hydrogen edge character and denoted as (*C-H). The G peak was fitted to a single BWF, and the baseline was approximated by a linear background, as shown in **Figure S14**. The combination of two Lorentzian functions and a BWF provided a profile with minimal fitting parameters that could effectively fit the Raman spectrum of the wide range of carbon materials with varying hydrogen content explored in this work. The BWF lineshape is given by:

$$I(\omega) = I_o \frac{[1 + (\omega - \omega_o/Q\Gamma)]^2}{1 + [(\omega - \omega_o)/\Gamma]^2} \qquad \text{(Equation 1)}$$

where I_o is the peak intensity, ω_o is the peak position, Γ is the FWHM, and Q is the BWF coupling coefficient. A negative Q value tails the BWF toward lower frequency and helps accounts for residual intensity between the D and G peaks. Due to the asymmetry of the BWF lineshape, ω_o does not lie at the frequency

of the peak maximum (ω_{max}) as in a simple Lorentzian or Gaussian function. To correct for this, the following equation was applied to determine ω_{max}:

$$\omega_{max} = \omega_o + \frac{\Gamma}{2Q} \qquad \text{(Equation 2)}$$

Since Q is negative, ω_{max} lies at a lower frequency than ω_o. FWHM(D) and FWHM(G) were determined based on FWHM of the Lorentzian associated with the D Peak and BWF fits, respectively. The position of the D peak (Pos(D)) was determined based on ω_o of the Lorentzian associated with the D Peak, and Pos(G) was determined based on ω_{max} of the BWF associated with the G peak by applying Equation 2.

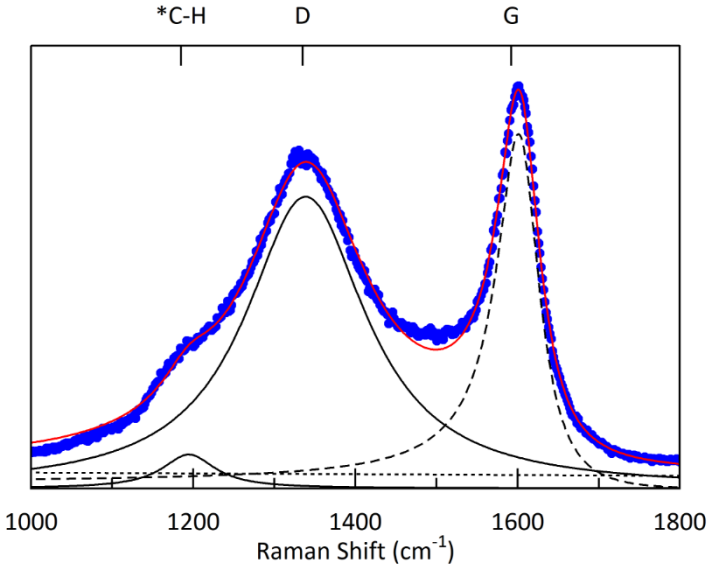

Figure S14. Representative fitting profile for the Raman spectrum of graphitic carbon. One Lorentzian (*C-H) is used to account for hydrogen edge character, a second Lorentzian (D) accounts for the D mode, and a BWF lineshape (G) accounts for the G mode.

X-Ray Absorption Spectroscopy. The boron chemical environments in each material were investigated by X-ray absorption spectroscopy (XAS) using synchrotron radiation at beam line BL8.0.1.4 at the Advanced Light Source (Lawrence Berkeley National Laboratory). The hand-ground samples were mounted on carbon tape and transferred into an ultrahigh vacuum (10^{-9} mbar) chamber for analysis. The total fluorescence yield (TFY) was measured to probe ~175 nm into the bulk of the sample, and the total

electron yield (TEY) was measured for analysis of the surface chemical environments. As reference materials, boron oxide (B_2O_3, 99.999%, Sigma-Aldrich), amorphous boron (98%, Alfa Aesar), hexagonal boron nitride (BN, 99.5%, Alfa Aesar), and boron carbide (~B_4C, 98%, Sigma-Aldrich) were also examined under identical conditions.

Scanning Electron Microscopy. Scanning electron microscopy (SEM) of the as-synthesized materials was performed for imaging using a field emission scanning electron microscope (SUPRA 55VP, ZEISS Group) operating at 1 kV with a working distance of < 5mm. Samples were prepared by mounting onto conductive carbon tape.

Energy Dispersive X-Ray Spectroscopy. Energy dispersive X-ray spectroscopy (EDX) was performed using a scanning electron microscope (PHI 710, Physical Electronics Inc.) under a focused electron beam with a well-defined energy of 10 kV operating at 10 nA. A windowless X-ray detector (XFlash 6|10, Bruker Corp.) was used, permitting the detection of boron. Samples were prepared by pressing the as-synthesized flakes into indium foil.

3. Computational Methods:

Decomposition Energy Estimations. The energy of decomposition of each molecular precursor, a proxy for its temperature of decomposition, was approximated as the difference in quantum mechanical electronic energy at 0 K (E^{SCF}) between the original precursor alone as compared to the sum of its elements in their standard state molecular form (e.g., H_2 gas for H, Cl_2 gas for Cl) or as monatomic gases for the solids (e.g., C gas for C, B gas for B):

$$\Delta E^{SCF} = \left(\sum_{i}^{elements} E_i^{SCF} \right) - E_{precursor}^{SCF} \qquad \text{(Equation 3)}$$

Hence, the Δ prefix carries the meaning of “decomposition” into the elements, typically either boron or carbon and the relevant diatomic gas (either hydrogen or halogen). Geometry optimization of each

species was performed independently, at a level of density functional theory (DFT) previously benchmarked[5] for investigations of adsorption systems containing carbon, boron, and hydrogen: the MN15 functional,[6] a meta nonseparable gradient approximation (meta-NGA) global hybrid for the exchange-correlation energy, combined with the def2-QZVPP basis set,[7] a high-quality quadruple zeta basis with two polarization functions, using a commercial computational chemistry software package (Gaussian 16[8]). Vibrational frequencies were then determined, which guaranteed the stability of the molecular structures and provided the electronic energies of the compounds of interest; standard thresholds for the single-point calculations, optimization, and frequency simulations were used. The final decomposition energy (ΔE^{SCF}) was then divided by the number of "solid" atoms (either B or C) in the sum to provide an estimate of the decomposition energy per atom, reported in units of eV atom^{-1}.

4. Materials Characterization of BC_x from Routes I-V

Morphology and Composition. The pyrolysis products of synthesis routes I–V varied significantly in terms of morphology and homogeneity. Representative SEM micrographs of the resulting morphologies of each product are shown in **Figure 2** of the main text. Likewise, the chemical compositions of the various morphologies produced during each pyrolysis reaction also varied, indicating different degrees of phase segregation (**Table S1**). As the benchmark for comparison, the co-pyrolysis of boron tribromide and benzene at 800 °C (route I) primarily results in free-standing flakes with a thickness of ~2 μm (**Figure 2a**), typically formed completely free from the walls of the quartz ampule. The surfaces of the flakes exhibit a cratered/dimpled topology that is characteristic of highly boron-doped graphitic carbons and other boron-rich phases.[1,4,9,10] Spheres with a diameter of ~2 μm are also present in minor abundance in route I. The boron-to-carbon ratio of both morphologies is ~0.21 (~BC_5) as measured using EDX, with only minor oxygen and bromine impurities (<5 at.%), consistent with previous studies.[1,4] We note that accurately determining the B:C ratio is challenging, and previous reports showing compositions closer to BC_3 were

evidenced by data collected using elastic recoil detection analysis (ERDA) which is highly suited to the quantification of light-element compositions compared to EDX.[1]

A comparable halide-free synthesis product to that of route I is achieved via the co-pyrolysis of sodium borohydride and benzene at 800 °C (route V). Using borohydride as a boron precursor requires a counter-ion, in this case sodium. To prevent the formation of metallic sodium, a sodium scavenger must be used. While a number of scavengers could be used, the additive used herein was iodine, leading to the formation of sodium iodide salt which is water soluble and hence easy to separate from the BC_x product. Route V also primarily produces flakes with a thickness of ~2 µm with a similar texture to those produced via route I, and which are also accompanied by spheres that range in diameter from 1–5 µm in minor abundance. The chemical composition of both flakes and spheres was effectively identical to that of the products of route I, with a boron to carbon ratio of ~0.22 (~BC_5 stoichiometry) and with little oxygen, sodium, or other contamination.

Table S1. Elemental composition (as determined by EDX) of each morphology of the BC_x products of synthesis routes I–V.

	Boron Precursor	**Flakes**	**Spheres**	**Fibers**	**Film**	**Carbide**
I	BBr_3	BC_5 (3% O, 3% Br)	BC_5 (3% O, 3% Br)	-	-	
II	B_2H_6	BC_3 (8% O)	B_2C (7% O)	BC_{32} (2% O)	-	
III	$B_{10}H_{14}$	BC_{19} (2% O)	BC_{10} (1% O)	-	B_5C_2 (4% O)	
IV	NDB	BC_7 (6% Cl, 3% O, 2% Al)	-	-	-	BC_5 (17% O, 5% Cl, 2% Al)
V	BH_4^-	BC_5 (4% O, 2% I)	BC_5 (1% O, 0.3% Na, 3% I)	-	-	

The products of synthesis route II (the co-pyrolysis of diborane and benzene at 700 °C) depart significantly from those of routes I and V, largely owing to the nature of the stainless-steel reactor. Route II yields a product with the largest degree of morphological variation of all synthesis routes explored herein. Fibers, spheres, and flakes, in order of descending contribution, are present in all parts of the product, regardless of whether collected exclusively from the thermowell (a cold head) or from the reactor base or walls. The fibers are likely a byproduct of metal-catalyzed side reactions on the stainless-steel body of the reactor, as described for other pyrolysis reactions carried out in the presence of Ni-containing steels.[11–13] The spheres produced by this synthesis are smooth in texture and vary in diameter from 1–5 μm. Contrary to routes I and V, these spheres are found to be composed primarily of boron, with a boron to carbon ratio of ~2 (B_2C) and a moderate oxygen content of 7 at.%. While fibers and spheres are the major morphologies generated by route II, flakes with a thickness of ~4 μm are also observed as a minor phase. These flakes are similar in appearance to those produced by routes I and V, exhibiting a cratered/dimpled texture and a boron to carbon ratio of ~0.4, close to that of BC_3.

Synthesis routes III and IV also lead to the formation of multiple morphologies. A colorful boron-rich film with a composition approaching B_4C is found on the surface of the layered graphitic flakes produced in route III. This layered structure is easily seen in the SEM images in **Figure 2c** of the main text. The underlying graphitic flakes contain only ~5 at.% boron (with very little oxygen incorporation). Meanwhile, the pyrolysis of NDB (route IV) also leads to the formation of two morphologies, one that is flake-like and another that exhibits the characteristic folded/crinkled textures indicative of boron carbide.[14] Interestingly, despite the outward appearance of the folded/crinkled regions, the elemental composition of both morphologies is close to that of the original NDB precursor molecule (BC_5), except with a large impurity content from not only oxygen (3-17 at.%) but also chlorine and aluminum (an additional 5-7 at.%). The large amount of oxygen contamination is typical of the products of other “molecular tiling”

routes, owing to the susceptibility of exposure to air during the requisite multistep organic synthesis of the tile; this disadvantage of tiling type synthesis routes has been previously discussed.[1]

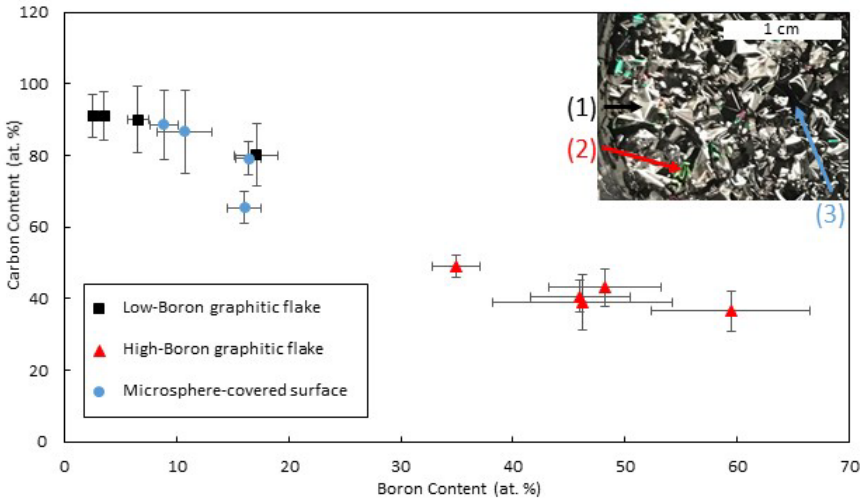

Figure S15. Compositional analysis of decaborane-derived BC_x (route III). Three morphologies can be seen: (1) low-boron content flakes with a grey metallic luster, (2) high-boron content flakes with a colorful metallic luster, and (3) microsphere-covered surfaces that appear dull black.

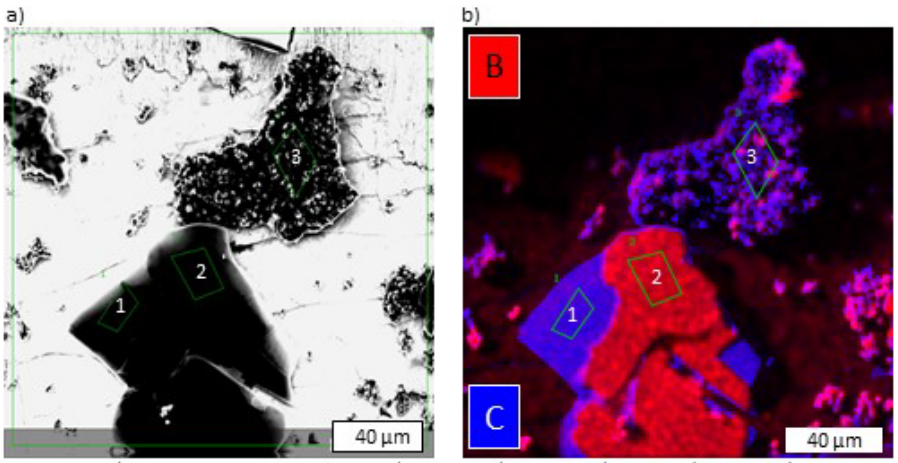

Sampling area	at.% C	at. % B	at. % O	at. % In
Low-Boron graphitic flake (1)	91.34	2.96	2.06	3.65
High-Boron graphitic flake (2)	48.03	35.86	13.70	2.42
Microspheres (3)	87.77	10.02	2.18	0.02

Figure S16. (a) SEM image and (b) EDX elemental map of decaborane-derived BCx (route III). The same heterogeneity observed by eye (**Figure S15**) can be quantifiably differentiated in terms of boron content.

Structure. XRD patterns and Raman spectra (E_L = 532 nm) of the pyrolysis products from synthesis routes I–V are shown in **Figure S17**. With the exception of route II, the "crystalline" products of all routes exhibit broad features consistent with that of turbostratic, nanocrystalline graphite. All of the products exhibit two dominant XRD peaks both consistent with graphite: the characteristic (002) reflection between 2θ = 25–26° that represents layer-to-layer ordering and a peak comprising the (10*l*) family of reflections centered at 2θ = 42–43° that is associated with in-plane ordering. Synthesis route II produces higher quality graphite, shown in XRD by the higher angle (002) reflection with a narrower FWHM compared to the other samples. This higher level of graphitic order is attributable to the catalytic activity of the metal reactor. All of the products also exhibit features primarily indicative of poorly-crystalline graphite: a G peak centered between 1570–1590 cm^{-1}, a D peak centered between 1335–1360 cm^{-1}, and a broad 2D region between 2500–3200 cm^{-1}. The products of routes III and IV also exhibit a low-frequency shoulder of the D peak between 1125–1250 cm^{-1} attributable to edge features of graphitic sheets terminated with hydrogen.[15] The product of route II is again an exception; two distinct types of Raman spectra were found upon spatial exploration of the heterogeneous morphologies present. The first spectral type (solid trace in **Figure S17b**) is consistent with that of other forms of graphitic BC_x phase-mixed with some content of elemental boron (as indicated by a series of peaks between 500–900 cm^{-1}). The second spectral type (dashed trace in **Figure S17b**) is consistent with a more ordered and lower boron-content graphitic carbon, consistent with the more ordered graphitic phase apparent in its XRD pattern. The D:G intensity ratio of this latter spectral type (~2:1) differs significantly from that of all other products and its 2D region comprises well-defined peaks centered at 2675 and 2930 cm^{-1}, revealing that synthesis route II produces a mixture of higher-quality low-boron-content graphite, and high-boron-content graphitic BC_x together with elemental boron.

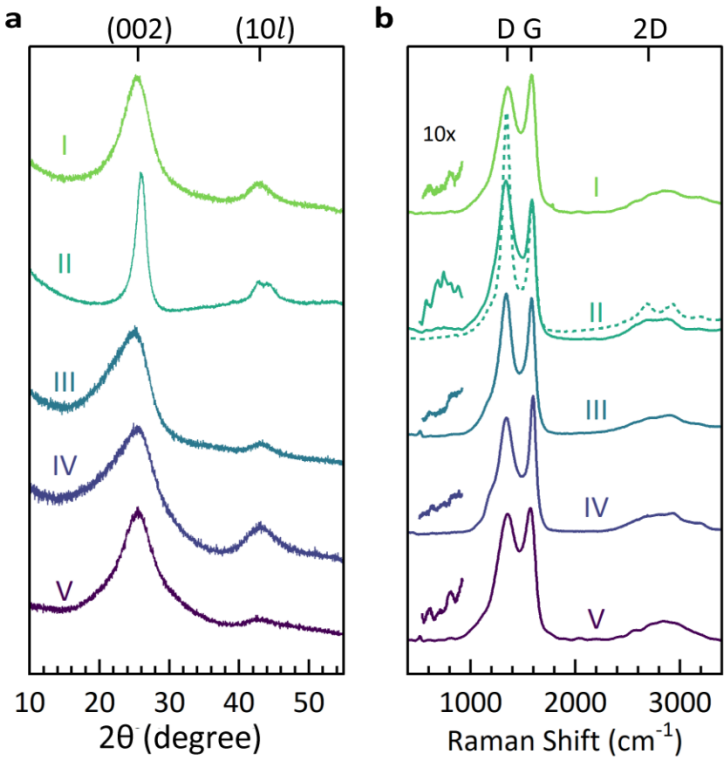

Figure S17. Structural analysis of the pyrolysis products from routes I-V. (a) XRD patterns and (b) Raman spectra (E_L = 532 nm) of boron tribromide- (I), diborane- (II), decaborane- (III), NDB- (IV), and sodium borohydride- (V) derived BC_x.

Boron Chemical Environments. The boron chemical environments produced in synthesis routes I–V were investigated by XAS, as shown in **Figure S18**. Several standard materials containing relevant boron chemical environments are shown in **Figure S18c** for reference. Hexagonal boron nitride (g-BN) contains ordered trigonal planar boron environments that are characterized by an intense π* transition at 191.6 eV, and a weaker σ* transition between 197–200 eV.[16] Amorphous boron (a-B) exhibits a broad, featureless absorption edge with an onset at 187–190 eV. Boron carbide (B_4C) exhibits the characteristic σ* transition originating from icosahedral boron (B_{12}) units at 190.6 eV.[17] Boron oxide (B_2O_3) exhibits an intense σ* transition associated with trigonal planar (BO_3) environments at 193.7 eV. This boron oxide environment is also observed in the other standard materials due to surface oxidation resulting from the extremely negative bond association energy of boron-oxygen bonds.

The boron K-edge XAS spectra of the products of routes I-V are shown in **Figure S18a** (enlarged in **Figure S18b**). Like the standards, all products exhibit a prominent boron oxide peak at 193.7 eV that is more intense in the TEY signal, consistent with the formation of a surface oxide layer. Synthesis route I primarily results in hexagonally-ordered trigonal planar BC_3 environments (g-BC_3) at 192.0 eV with a small contribution from amorphous BC_3 (a-BC_3) at 189.4 eV, in agreement with previous studies.[4] The surface (TEY) and bulk (TFY) signals are highly consistent, indicating a homogeneous single-phase product. Synthesis route V produces a similar distribution of boron environments as route I, with a primary contribution from g-BC_3 at 192.0 eV. The product of route V produces a small but detectable contribution from icosahedral B_{12} environments centered at 190.6 eV and a smaller contribution from boron oxide type environments than for the product of route I.

Synthesis routes II-IV produce drastically different chemical environments at the surface compared to within the bulk of the sample, consistent with the morphological heterogeneity revealed by SEM, XRD, and Raman spectroscopy. By comparison of the TEY and TFY spectra of the product of route II, a core-shell structure with a core consisting of elemental boron and a shell of graphitic carbon that contains an array of substitutional boron atoms is revealed. Synthesis route III also produces XAS features consistent with a core-shell structure. The surface spectrum exhibits a sloping edge with a feature at 190.8 eV associated with icosahedral B_{12} environments as well as a distinct feature at 192.3 eV that is associated with sub-stoichiometric boron carbide domains arising from the inclusion of carbon into the nest-like structure of the decaborane precursor.[18] The bulk of the sample is a combination of elemental boron, boron carbide (indicated by a subtle feature at 190.8 eV), and sub-stoichiometric boron carbide domains. Synthesis route IV produces a prominent feature from boron oxide at 193.7 eV throughout its core-shell structure, containing predominantly a-BC_3 and sub-stoichiometric boron carbide environments in the core with almost exclusively sub-stoichiometric carbide in the shell.

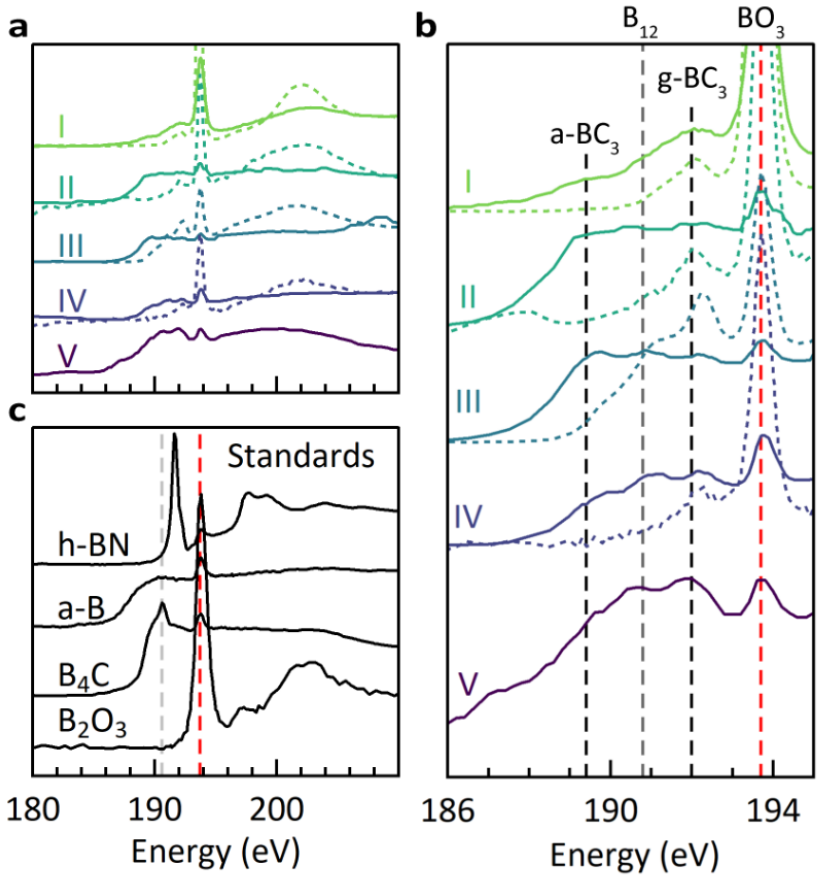

Figure S18. XAS spectra near the B K-edge of the pyrolysis products from routes I-V and related reference materials. The samples shown are boron tribromide- (I), diborane- (II), decaborane- (III), NDB- (IV), and sodium borohydride- (V) derived BC_x, hexagonal boron nitride, amorphous boron, boron carbide, and boron oxide. TEY spectra (surface) are shown as dashed lines, and TFY spectra (bulk) as solid lines.

Raman spectroscopy at multiple wavelengths was used to determine the magnitude of the dispersion of the D peak in the products of routes I-V, as shown in **Figures S19-S23** and summarized in **Table S2**. A lower dispersion of the D peak is indicative of higher contents of C_6B_6 "flower-like" units within the planar structure of the graphitic parts of a given BC_x product. Raman and XAS analysis of the products of synthesis routes I and V both corroborate a large contribution from g-BC_3 environments throughout the bulk of the sample; the D peak dispersion (Disp(D)) of the product of route V is the lowest of all samples measured herein. The products of route II (from diborane) showed two distinct Raman spectral types, each with a

distinct Disp(D) as well. One environment is remarkably similar to that of the products of routes I and V and appears to be akin to bulk BC_3.; this is in agreement with the XAS spectrum (**Figure S18**) which reveals that the surface of the product of route II exhibits a high density of g-BC_3 environments. The other environment is typical of ordered, boron-poor graphitic carbon, likely catalyzed by the metal walls of the reactor. The Raman spectra of the product of synthesis route III (derived from $B_{10}H_{14}$) were spatially homogeneous and exhibit a Disp(D) of 33 cm^{-1} eV^{-1} indicating a detectable presence of g-BC_3. The core-shell nature of this sample is strongly evidenced by the XAS results (see above). Lastly, the product of synthesis route IV exhibits a Raman spectrum that resembles that of a standard disordered carbon, with a Disp(D) of 44 cm^{-1} eV^{-1}. This is expectable on the basis of the fact that the naphthalene moiety of the NDB precursor would need to be at least partially decomposed to produce hexagonally ordered g-BC_3 environments; the B–C bonds in the original molecular structure are not in the correct position for true molecular tiling. The pyrolysis temperature of route IV (800 °C) is likely too low to decompose the aromatic structure of naphthalene. The XAS spectra of the route IV product also show discrepancies between the surface and bulk boron environments, indicating the likely liberation of the bridging diborane during pyrolysis.

Table S2. Raman D peak dispersion as a function of Reaction number and boron reagent utilized in the pyrolysis reaction.

	Boron Precursor	**Disp(D) (cm^{-1} eV^{-1})**
I	BBr_3	32
II	B_2H_6	21, 43
III	$B_{10}H_{14}$	33
IV	NDB	44
V	BH_4^-	13

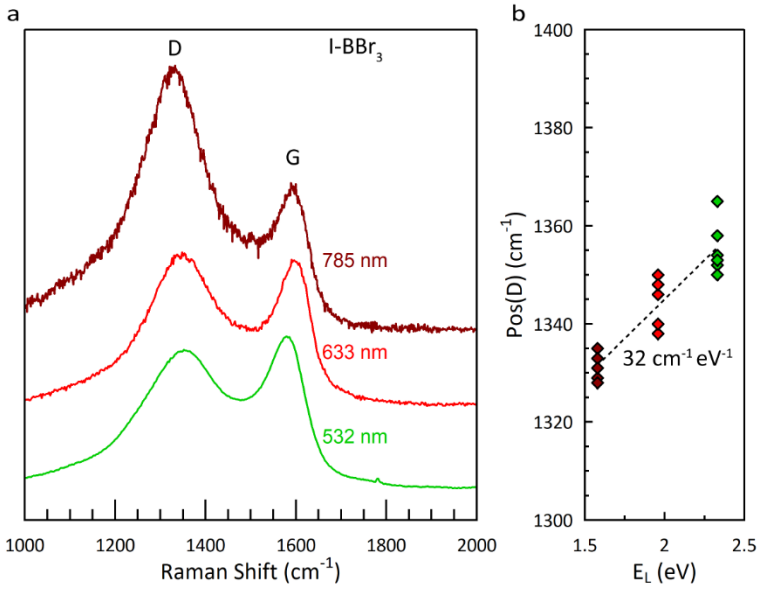

Figure S19. Raman analysis of the D peak dispersion of the product of the co-pyrolysis of BBr_3 and C_6H_6 at 800 °C (route I). (a) Representative Raman spectra at 532 nm, 633 nm, and 785 nm. (b) D peak position as a function of excitation wavelength, and the least-squares fit dispersion relation.

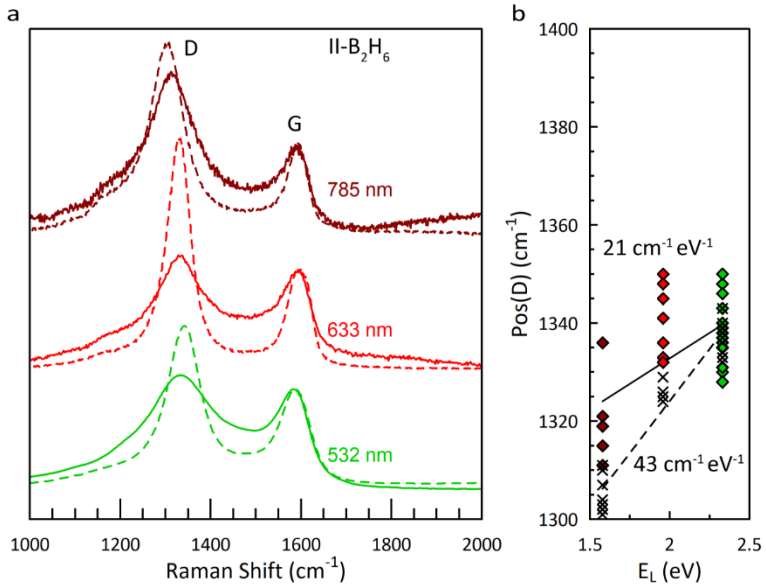

Figure S20. Raman analysis of the D peak dispersion of the product of the co-pyrolysis of B_2H_6 and C_6H_6 at 700 °C (route II). (a) Representative Raman spectra at 532 nm, 633 nm, and 785 nm. (b) D peak position as a function of excitation wavelength, and the least-squares fit dispersion relation.

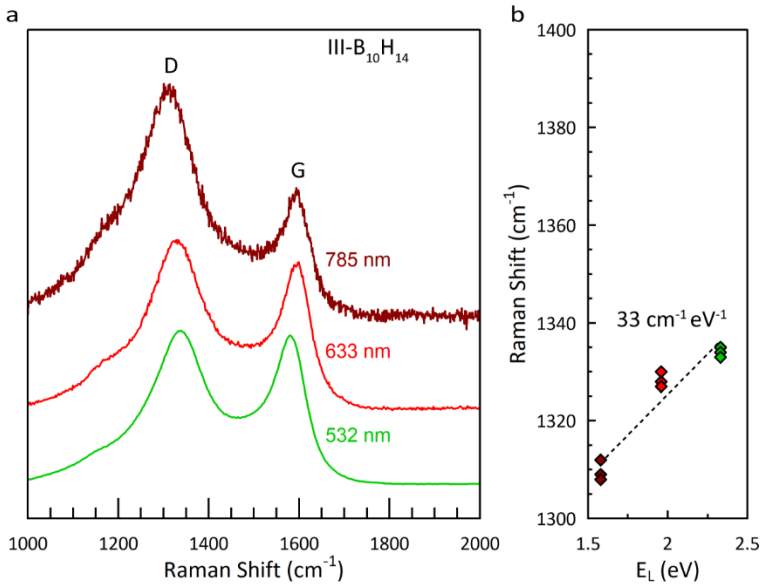

Figure S21. Raman analysis of the D peak dispersion of the product of the co-pyrolysis of $B_{10}H_{14}$ and C_6H_6 at 800 °C (route III). (a) Representative Raman spectra at 532 nm, 633 nm, and 785 nm. (b) D peak position as a function of excitation wavelength, and the least-squares fit dispersion relation.

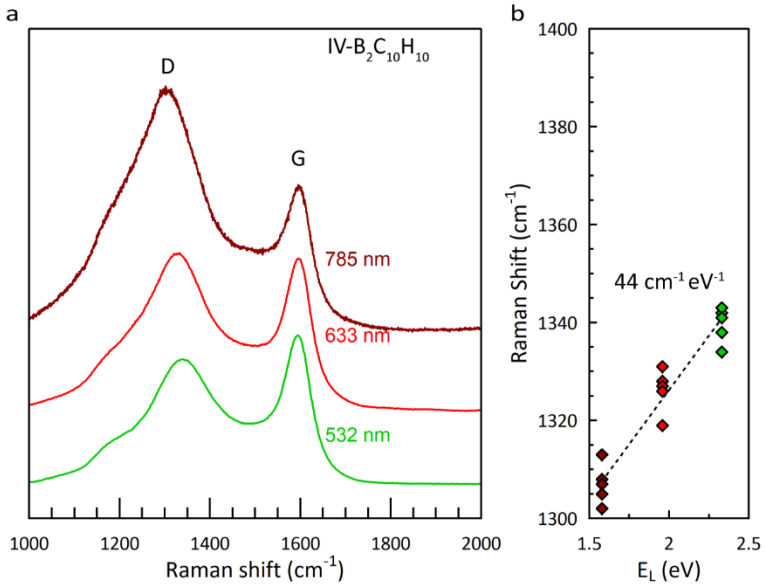

Figure S22. Raman analysis of the D peak dispersion of the product of the pyrolysis of $B_2C_{10}H_{14}$ (NDB) at 800 °C (route IV). (a) Representative Raman spectra at 532 nm, 633 nm, and 785 nm. (b) D peak position as a function of excitation wavelength, and the least-squares fit dispersion relation.

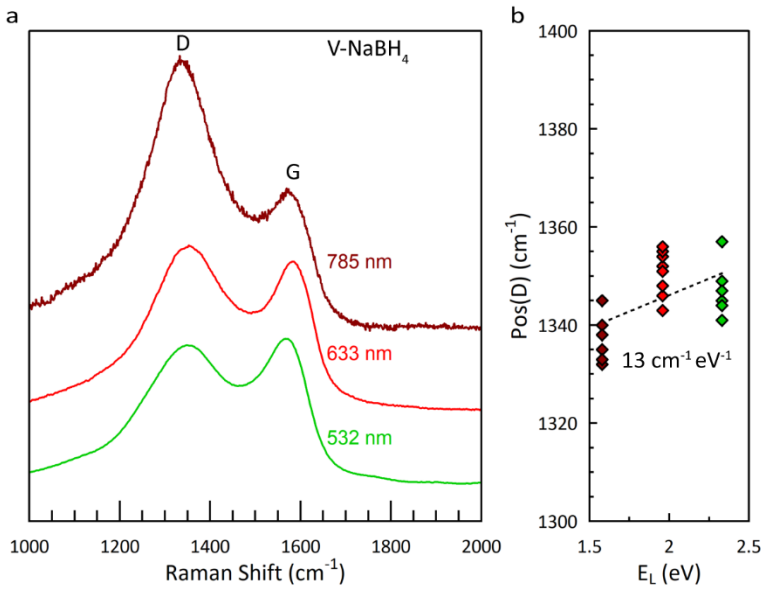

Figure S23. Raman analysis of the D peak dispersion of the product of the co-pyrolysis of $NaBH_4$ and C_6H_6 at 800 °C (route V). (a) Representative Raman spectra at 532 nm, 633 nm, and 785 nm. (b) D peak position as a function of excitation wavelength, and the least-squares fit dispersion relation.

5. Computational Results:

Decomposition Energy/Temperature Correlation. The relative thermochemical stabilities of the precursor molecules explored in this work were roughly approximated by the simple DFT approach described in Section 3 above. The resulting decomposition energies (ΔE^{SCF}) of several common B- and C-containing precursors are shown in **Table S3**. The relationship between ΔE^{SCF} and the experimental decomposition temperature (T_d) of the same precursors is shown in **Figure S24**. Benzene is calculated to exhibit a decomposition energy of 9.1 eV per carbon atom, which corresponds to an experimental decomposition temperature of ~750 °C.[19] The decomposition energy of boron tribromide is similar to that of benzene: 8.8 eV per boron atom. Of the halide-free precursors, borohydride exhibits the most similar decomposition energy to benzene: 7.0 eV per boron atom. Diborane and decaborane are found to be less stable, at 6.2 and 6.3 eV per boron atom, respectively. These values are consistent with the low stability and high reactivity characteristic of the entire family of lower boranes.[20] It is notable that the

decomposition energy of NDB ($B_2C_{10}H_{10}$) is significantly higher at 8.5 eV per atom, normalized to the sum of both boron and carbon within the single precursor; this gives rise to an expected decomposition temperature of ~600 °C according to the fit over all precursors investigated (dashed line).

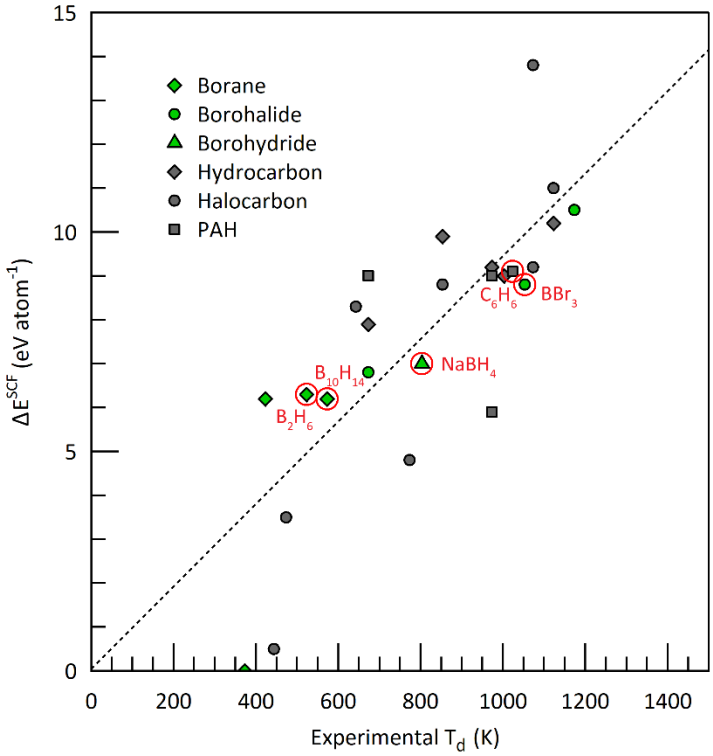

Figure S24. Thermochemical decomposition energy/temperature correlation. Calculated decomposition energy (ΔE^{SCF}), normalized to the number of atoms of relevance (B or C), as a function of experimental decomposition temperature (T_d), showing an expectable correlation that passes close to the origin. The precursors explored in this work are circled in red and indicated with their molecular formula. Note: the "decomposition temperature" of any species is highly dependent on the experimental method/apparatus used, as well as the definition of decomposition itself.

Table S3. Decomposition energies (ΔE^{SFC}), experimental decomposition temperatures, and corresponding references for small molecules of interest in co-pyrolysis reactions to produce boron- and carbon-containing products.

Decomposition Reaction	ΔE^{SFC}* (eV atom^{-1})	Experimental T_d (°C)	Experimental SI Reference
$BF_3 \rightarrow B + 3/2\ F_2$	18.3	-	-
$CF_4 \rightarrow C + 2\ F_2$	13.8	800	21
$C_6F_6 \rightarrow 6\ C + 3\ F_2$	11.0	850	22
$BCl_3 \rightarrow B + 3/2\ Cl_2$	10.5	900	23
$CH_4 \rightarrow C + 2\ H_2$	10.2	850	24,25
$C_2H_6 \rightarrow 2\ C + 3\ H_2$	9.9	580	26
$C_3H_6 \rightarrow 3\ C + 3\ H_2$	9.2	700	27
$C_6Cl_6 \rightarrow 6\ C + 3\ Cl_2$	9.2	800	28
$C_6H_6 \rightarrow 6\ C + 3\ H_2$	9.1	750	19
$C_{10}H_{10} \rightarrow 10\ C + 5\ H_2$	9.0	400	29
$C_2H_4 \rightarrow 2\ C + 2\ H_2$	9.0	730	30
$C_{24}H_{12} \rightarrow 24\ C + 6\ H_2$	9.0	700	this work
$C_6Br_6 \rightarrow 6\ C + 3\ Br_2$	8.8	580	31
$BBr_3 \rightarrow B + 3/2\ Br_2$	8.8	780	32
$C_6I_6 \rightarrow 6\ C + 3\ I_2$	8.3	370	33
$C_2H_2 \rightarrow 2\ C + H_2$	7.9	400	34
$BH_4^- \rightarrow B + 2\ H_2 + e^-$	7.0	530	35
$BI_3 \rightarrow B + 3/2\ I_2$	6.8	400	36,37
$B_{10}H_{14} \rightarrow 10\ B + 7\ H_2$	6.3	250	38
$B_5H_9 \rightarrow 5\ B + 9/2\ H_2$	6.2	150	38
$B_2H_6 \rightarrow 2\ B + 3\ H_2$	6.2	100-300	27,39,40
$C_{10}H_8 \rightarrow 10\ C + 4\ H_2$	5.9	700	41
$CCl_4 \rightarrow C + 2\ Cl_2$	4.8	500	42
$CBr_4 \rightarrow C + 2\ Br_2$	3.5	200	43
$Cl_4 \rightarrow C + 2\ I_2$	0.5	-	-

*Note: total decomposition energy is normalized per heteroatom of relevance (C or B)

6. Supporting References:

(1) Stadie, N. P.; Billeter, E.; Piveteau, L.; Kravchyk, K. V.; Döbeli, M.; Kovalenko, M. V. Direct Synthesis of Bulk Boron-Doped Graphitic Carbon. *Chem. Mater.* **2017**, *29* (7), 3211–3218. https://doi.org/10.1021/acs.chemmater.7b00376.

(2) Scholz, A. S.; Massoth, J. G.; Bursch, M.; Mewes, J.-M.; Hetzke, T.; Wolf, B.; Bolte, M.; Lerner, H.-W.; Grimme, S.; Wagner, M. BNB-Doped Phenalenyls: Modular Synthesis, Optoelectronic Properties, and One-Electron Reduction. *J. Am. Chem. Soc.* **2020**, *142* (25), 11072–11083. https://doi.org/10.1021/jacs.0c03118.

(3) Ferrari, A. C.; Basko, D. M. Raman Spectroscopy as a Versatile Tool for Studying the Properties of Graphene. *Nat. Nanotechnol.* **2013**, *8* (4), 235–246. https://doi.org/10.1038/nnano.2013.46.

(4) McGlamery, D.; Baker, A. A.; Liu, Y.-S.; Mosquera, M. A.; Stadie, N. P. Phonon Dispersion Relation of Bulk Boron-Doped Graphitic Carbon. *J. Phys. Chem. C* **2020**, *124* (42), 23027–23037. https://doi.org/10.1021/acs.jpcc.0c06918.

(5) Rowsey, R.; Taylor, E. E.; Irle, S.; Stadie, N. P.; Szilagyi, R. K. Methane Adsorption on Heteroatom-Modified Maquettes of Porous Carbon Surfaces. *J. Phys. Chem. A* **2021**, *125* (28), 6042–6058. https://doi.org/10.1021/acs.jpca.0c11284.

(6) Yu, H. S.; He, X.; Li, S. L.; Truhlar, D. G. MN15: A Kohn–Sham Global-Hybrid Exchange–Correlation Density Functional with Broad Accuracy for Multi-Reference and Single-Reference Systems and Noncovalent Interactions. *Chem. Sci.* **2016**, *7* (8), 5032–5051. https://doi.org/10.1039/C6SC00705H.

(7) Weigend, F.; Ahlrichs, R. Balanced Basis Sets of Split Valence, Triple Zeta Valence and Quadruple Zeta Valence Quality for H to Rn: Design and Assessment of Accuracy. *Phys. Chem. Chem. Phys.* **2005**, *7* (18), 3297–3305. https://doi.org/10.1039/B508541A.

(8) Frisch, M. J.; Trucks, G. W.; Schlegel, H. B.; Scuseria, G. E.; Robb, M. A.; Cheeseman, J. R.; Scalmani, G.; Barone, V.; Petersson, G. A.; Nakatsuji, H.; Li, X.; Caricato, M.; Marenich, A. V.; Bloino, J.; Janesko, B. G.; Gomperts, R.; Mennucci, B.; Hratchian, H. P.; Ortiz, J. V.; Izmaylov, A. F.; Sonnenberg, J. L.; Williams-Young, D.; Ding, F.; Lipparini, F.; Egidi, F.; Goings, J.; Peng, B.; Petrone, A.; Henderson, T.; Ranasinghe, D.; Zakrzewski, V. G.; Gao, J.; Rega, N.; Zheng, G.; Liang, W.; Hada, M.; Ehara, M.; Toyota, K.; Fukuda, R.; Hasegawa, J.; Ishida, M.; Nakajima, T.; Honda, Y.; Kitao, O.; Nakai, H.; Vreven, T.; Throssell, K.; Montgomery, J. A., Jr.; Peralta, J. E.; Ogliaro, F.; Bearpark, M. J.; Heyd, J. J.; Brothers, E. N.; Kudin, K. N.; Staroverov, V. N.; Keith, T. A.; Kobayashi, R.; Normand, J.; Raghavachari, K.; Rendell, A. P.; Burant, J. C.; Iyengar, S. S.; Tomasi, J.; Cossi, M.; Millam, J. M.; Klene, M.; Adamo, C.; Cammi, R.; Ochterski, J. W.; Martin, R. L.; Morokuma, K.; Farkas, O.; Foresman, J. B.; Fox, D. J. *Gaussian 16*, **2016**.

(9) Cermignani, W.; Paulson, T. E.; Onneby, C.; Pantano, C. G. Synthesis and Characterization of Boron-Doped Carbons. *Carbon* **1995**, *33* (4), 367–374. https://doi.org/10.1016/0008-6223(94)00160-2.

(10) Wallenberger, F. T.; Nordine, P. C. Strong, Small Diameter, Boron Fibers by LCVD. *Mater. Lett.* **1992**, *14* (4), 198–202. https://doi.org/10.1016/0167-577X(92)90156-E.

(11) Toebes, M. Impact of the Structure and Reactivity of Nickel Particles on the Catalytic Growth of Carbon Nanofibers. *Catal. Today* **2002**, *76* (1), 33–42. https://doi.org/10.1016/S0920-5861(02)00209-2.

(12) Tzeng, S.-S.; Hung, K.-H.; Ko, T.-H. Growth of Carbon Nanofibers on Activated Carbon Fiber Fabrics. *Carbon* **2006**, *44* (5), 859–865. https://doi.org/10.1016/j.carbon.2005.10.033.

(13) De Jong, K. P.; Geus, J. W. Carbon Nanofibers: Catalytic Synthesis and Applications. *Catal. Rev.* **2000**, *42* (4), 481–510. https://doi.org/10.1081/CR-100101954.

(14) Sha, W.; Liu, Y.; Zhou, Y.; Huang, Y.; Huang, Z. Effect of Carbon Content on Mechanical Properties of Boron Carbide Ceramics Composites Prepared by Reaction Sintering. *Materials* **2022**, *15* (17), 6028. https://doi.org/10.3390/ma15176028.

(15) Yamada, Y.; Kawai, M.; Yorimitsu, H.; Otsuka, S.; Takanashi, M.; Sato, S. Carbon Materials with Zigzag and Armchair Edges. *ACS Appl. Mater. Interfaces* **2018**, *10* (47), 40710–40739. https://doi.org/10.1021/acsami.8b11022.
(16) Jiménez, I.; Sutherland, D. G. J.; van Buuren, T.; Carlisle, J. A.; Terminello, L. J.; Himpsel, F. J. Photoemission and X-Ray-Absorption Study of Boron Carbide and Its Surface Thermal Stability. *Phys. Rev. B* **1998**, *57* (20), 13167–13174. https://doi.org/10.1103/PhysRevB.57.13167.
(17) Caretti, I.; Gago, R.; Albella, J. M.; Jiménez, I. Boron Carbides Formed by Coevaporation of B and C Atoms: Vapor Reactivity, $B_xC_{(1-x)}$ Composition, and Bonding Structure. *Phys. Rev. B* **2008**, *77* (17), 174109. https://doi.org/10.1103/PhysRevB.77.174109.
(18) Pallier, C.; Leyssale, J.-M.; Truflandier, L. A.; Bui, A. T.; Weisbecker, P.; Gervais, C.; Fischer, H. E.; Sirotti, F.; Teyssandier, F.; Chollon, G. Structure of an Amorphous Boron Carbide Film: An Experimental and Computational Approach. *Chem. Mater.* **2013**, *25* (13), 2618–2629. https://doi.org/10.1021/cm400847t.
(19) Zanetti, J. E.; Egloff, G. The Thermal Decomposition of Benzene. *J. Ind. Eng. Chem.* **1917**, *9* (4), 350–356. https://doi.org/10.1021/ie50088a009.
(20) Long, L. H. The Mechanisms of Thermal Decomposition of Diborane and of Interconversion of the Boranes: A Reinterpretation of the Evidence. *J. Inorg. Nucl. Chem.* **1970**, *32* (4), 1097–1115. https://doi.org/10.1016/0022-1902(70)80104-X.
(21) *Carbon Tetrafluoride*. https://www.chembk.com/en/chem/carbon%20tetrafluoride (accessed 2023-07-01).
(22) Dibeler, V. H.; Reese, R. M.; Mohler, F. L. Ionization and Dissociation of Hexafluorobenzene by Electron Impact. *J. Chem. Phys.* **1957**, *26* (2), 304–305. https://doi.org/10.1063/1.1743288.
(23) Muroi, M.; Otani, M.; Habuka, H. Boron-Silicon Film Chemical Vapor Deposition Using Boron Trichloride, Dichlorosilane and Monomethylsilane Gases. *ECS J. Solid State Sci. Technol.* **2021**, *10* (6), 064006. https://doi.org/10.1149/2162-8777/ac08d6.
(24) Yousefi, M.; Donne, S. Experimental Study for Thermal Methane Cracking Reaction to Generate Very Pure Hydrogen in Small or Medium Scales by Using Regenerative Reactor. *Front. Energy Res.* **2022**, *10*, 971383. https://doi.org/10.3389/fenrg.2022.971383.
(25) Guéret, C.; Daroux, M.; Billaud, F. Methane Pyrolysis: Thermodynamics. *Chem. Eng. Sci.* **1997**, *52* (5), 815–827. https://doi.org/10.1016/S0009-2509(96)00444-7.
(26) Laidler, K. J.; Wojciechowski, B. W.; Steacie, E. W. R. Kinetics and Mechanisms of the Thermal Decomposition of Ethane - I. The Uninhibited Reaction. *Proc. R. Soc. Lond. A* **1961**, *260* (1300), 91–102. https://doi.org/10.1098/rspa.1961.0015.
(27) Hurd, D. T. The Reactions of Diborane with Hydrocarbons. *J. Am. Chem. Soc.* **1948**, *70* (6), 2053–2055. https://doi.org/10.1021/ja01186a020.
(28) Ahling, B.; Lindskog, A. Thermal Destruction of PCB and Hexachlorobenzene. *Sci. Total Environ.* **1978**, *10* (1), 51–59. https://doi.org/10.1016/0048-9697(78)90049-9.
(29) Straus, S.; Madorsky, S. L. Thermal Stability of Polydivinylbenzene and of Copolymers of Styrene With Divinylbenzene and With Trivinylbenzene. *J. Res. NBS A Phys. Chem.* **1961**, *65A* (3), 243–248. https://doi.org/10.6028/jres.065A.029.
(30) Towell, G. D.; Martin, J. J. Kinetic Data from Nonisothermal Experiments: Thermal Decomposition of Ethane, Ethylene, and Acetylene. *AIChE J.* **1961**, *7* (4), 693–698. https://doi.org/10.1002/aic.690070432.
(31) Jiang, L.; Niu, T.; Lu, X.; Dong, H.; Chen, W.; Liu, Y.; Hu, W.; Zhu, D. Low-Temperature, Bottom-Up Synthesis of Graphene via a Radical-Coupling Reaction. *J. Am. Chem. Soc.* **2013**, *135* (24), 9050–9054. https://doi.org/10.1021/ja4031825.

(32) Sugaya, T.; Takeuchi, Y.; Watanabe, O. Preparation and Crystal Structure of Solid Boron Grown from the BBr_3-H_2 Mixture. *J. Common Met.* **1976**, *47*, 49–54. https://doi.org/10.1016/0022-5088(76)90073-4.
(33) Mattern, D. L. Periodination of Benzene with Periodate/Iodide. *J. Org. Chem.* **1983**, *48* (24), 4772–4773. https://doi.org/10.1021/jo00172a063.
(34) Cullis, C. F.; Franklin, N. H.; Gaydon, A. G. The Pyrolysis of Acetylene at Temperatures from 500 to 1000 °C. *Proc. R. Soc. Lond. A* **1964**, *280* (1380), 139–152. https://doi.org/10.1098/rspa.1964.0136.
(35) Martelli, P.; Caputo, R.; Remhof, A.; Mauron, P.; Borgschulte, A.; Züttel, A. Stability and Decomposition of $NaBH_4$. *J. Phys. Chem. C* **2010**, *114* (15), 7173–7177. https://pubs.acs.org/doi/full/10.1021/jp909341z.
(36) Moore, R. E.; Ownby, P. D. Thermal Decomposition of Boron Triiodide on Molybdenum Field Emitter Surfaces. *Jpn. J. Appl. Phys.* **1974**, *13* (S2), 71. https://doi.org/10.7567/JJAPS.2S2.71.
(37) Gao, W. Crystal Growth of Alpha-Rhombohedral Boron. Thesis, Kansas State University, 2010. https://krex.k-state.edu/handle/2097/4171 (accessed 2023-07-01).
(38) Owen, J. The Pyrolysis of Decaborane. *J. Chem. Soc.* **1961**, 5438–5444. https://doi.org/10.1039/JR9610005438.
(39) Travers, M. W. On the New View of the Nature of the Covalent Linkage, and the Formation of Free Radicals. *Trans. Faraday Soc.* **1934**, *30* (0), 100–102. https://doi.org/10.1039/TF9343000100.
(40) Mazaheri, A.; Javadi, M.; Abdi, Y. Chemical Vapor Deposition of Two-Dimensional Boron Sheets by Thermal Decomposition of Diborane. *ACS Appl. Mater. Interfaces* **2021**, *13* (7), 8844–8850. https://doi.org/10.1021/acsami.0c22580.
(41) Gai, C.; Dong, Y.; Yang, S.; Zhang, Z.; Liang, J.; Li, J. Thermal Decomposition Kinetics of Light Polycyclic Aromatic Hydrocarbons as Surrogate Biomass Tar. *RSC Adv.* **2016**, *6* (86), 83154–83162. https://doi.org/10.1039/C6RA15513H.
(42) Tonnoir, H.; Huo, D.; Davoisne, C.; Celzard, A.; Fierro, V.; Saurel, D.; El Marssi, M.; Benyoussef, M.; Meunier, P.; Janot, R. Pyrolysis Temperature Dependence of Sodium Storage Mechanism in Non-Graphitizing Carbons. *Carbon* **2023**, *208*, 216–226. https://doi.org/10.1016/j.carbon.2023.03.055.
(43) Hoke, W. E.; Weir, D. G.; Lemonias, P. J.; Hendriks, H. T. Carbon Tetrabromide Carbon Doping of Molecular Beam Epitaxial (GaAs) Films. *Appl. Phys. Lett.* **1994**, *64* (2), 202–204. https://doi.org/10.1063/1.111504.